Friction
https://doi.org/10.1007/s40544-023-0771-5
ISSN 2223-7690
CN 10-1237/TH
RESEARCH ARTICLE

Wear behavior of copper material removal during fluid jet polishing: A comparative study between experiment and simulation

Wenjing ZHANG[1], Xin ZHANG[1,*], Tiancheng AI[1], Dan GUO[1,*], Guoshun PAN[1,2,*]

[1] *State Key Laboratory of Tribology in Advanced Equipment, Tsinghua University, Beijing 100084, China*

[2] *Guangdong Provincial Key Laboratory of Optomechatronics, Shenzhen 518057, China*

Received: 15 March 2023 / Revised: 05 April 2023 / Accepted: 21 April 2023

Abstract: As a crucial part in micro-electromechanical manufacture, local ultra-precision processing of highly ductile copper is expected to be realized by fluid jet polishing (FJP), which widely utilized in optical elements. Since copper exhibits different wear behavior from stiff and brittle material, there is currently no abrasive wear prediction model applicable for copper to investigate the polishing mechanism. This research reveals that the copper material removal is dominated by deformation wear rather than cutting wear through abrasive jet impact experiments and localized wear scars analysis. A three-dimensional gas-liquid-particle triphasic wear model for copper in FJP is developed by considering impact energy and wear mechanism simultaneously. Ultimately, validation assessments at various working pressures and impingement angles achieve the goodness-of-fit up to 0.92–0.97 in quantitative comparison between simulations and experimental measurements, which demonstrate the wear prediction ability of the proposed model. This investigation facilitates a better understanding of copper wear mechanism and provides theoretical guidance for FJP process optimization.

Keywords: fluid jet polishing (FJP); wear mechanism; computational fluid mechanics; wear model; material removal

1 Introduction

As a non-contact polishing technology, fluid jet polishing (FJP) has been extensively utilized for the advantages of superior shape adaptation in machining complex surfaces [1–3]. Since FJP was first attempted by using premixed slurry (water containing 21.8 μm-sized silicon carbide abrasive) at a low pressure to realize the local shaping and polishing of BK7 glass device surfaces [4, 5], it has been proved to polish brittle optical elements to a roughness less than 1 nm and applied to cavities and microgrooves [1, 6, 7]. Up to now, efficient roughness reduction has also been achieved by FJP in metallic materials, like aluminum and nickel-copper alloys [8, 9]. For high ductility metal like copper, which is significantly applied in micro-electromechanical systems, chemical mechanical planarization (CMP) is the dominant mean for global flattening [10–12]. However, obvious limitations of CMP are exposed when processing local and microstructural functional surfaces [13, 14]. Hence, FJP holds great potential for copper ultra-precision polishing to complement with CMP.

During FJP process, the material removal rate distribution is influenced by the size of slurry jet acting as the polishing tool, which is characterized as wear behavior and named as tool influence function (TIF) [15, 16]. With changes in flow field distribution and particle motion, key parameters need to be considered for a suitable TIF construction [17–19],

* Corresponding authors: Xin ZHANG, E-mail: zx20@tsinghua.org.cn; Dan GUO, E-mail: guodan26@tsinghua.edu.cn; Guoshun PAN, E-mail: pangs@tsinghua.edu.cn

Nomenclature

V_p	Particle velocity	$f(\alpha)$	Particle impact angle dependence of wear damage
t	Time	α	Impact angle between particle and workpiece surface
F_D	Drag force per unit particle mass	K	Constant regulated the wear depth
U	Fluid velocity	Hv	Vickers hardness of the workpiece material
g	Acceleration of gravity	V^*	Reference impact velocity
ρ_p	Particle density	d^*	Reference particle diameter
ρ	Fluid density	k_1	Coefficient related to hardness
F	Additional forces	k_2	Coefficient related to impact velocity
μ	Fluid dynamic viscosity	k_3	Coefficient related to particle diameter
d_p	Particle diameter	n_1, n_2	Coefficient related to particle impact angle
Re	Reynolds number	S_1, q_1, S_2, q_2	Coefficient related to impact conditions
C_D	Drag coefficient		
$E(\alpha)$	Material volume removed per mass of particles		
E_{90}	Material removal under normal particle impact		

including particle properties (e.g. material, shape, size), workpiece properties (e.g. material, structure, curvature), and the impact information between particles and workpiece surface (e.g. impact velocity, impact angle, number of repeated impacts of particles) [3, 20, 21]. Unfortunately, the experiments are conducted in a confined space since severe splash and turbulence effects occur when the slurry jet impinges the workpiece surface, which creates difficulties in the observation of flow field. Intractable problems are faced in detection of impact information by experimental means alone due to shortages of current monitor methods, such that a computational tool is required to simulate the flow field motion and predict the wear behavior [22].

For TIF construction, the impact information is extracted by means of computational fluid dynamics and substituted into the specified wear model, ultimately allowing for the calculation of TIF shape [23]. Over the past few decades, several wear models have been proposed to investigate wear behavior in various applications such as bends and jets [24, 25]. The first abrasive wear model was established by Finnie to realize cutting wear formula deduction of a single silicon carbide particle, which achieved effective wear calculation at low impact angles [26]. Bitter supplemented the limitation of Finnie model for high impact angle calculation based on energy balance equation and Hertz contact theory, and assumed that the particle wear behavior was integrated cutting wear with deformation wear [27]. This assumption had been proven effective through numerous research projects on the abrasive wear issue, leading to the development of a series of theoretical wear models [22, 28, 29]. Moreover, creative empirical wear models based on premixed slurry impingement experiments with gas-particle flow or liquid-particle flow were proposed and optimized [30–33]. Especially, a semi-empirical wear model proposed by Oka et al. was verified to be suitable for application to slurry jet impingement tests with clear parameter forms and broad material adaptations [34, 35]. In addition, the formulas and coefficients in Oka model were assigned to physical meaning of wear mechanism, which was extremely beneficial and reliable for the extended study of various materials wear. However, the wear model of copper impacted by aluminum oxide particles during FJP process has not been reported. It is necessary to explore Oka model deeply and adapt the coefficients appropriately [36].

Emphasized on the wear behavior, this work aimed at comparative analysis of wear profile on copper surface between jet impact experiments of micro-sized particles (0.36–13.18 μm) and numerical simulations of gas-liquid-particle flow, which demonstrated that the material removal characteristics of copper are distinctly different from stiff and brittle materials. By analyzing the local wear scars on copper surface, a quantitative wear prediction model applicable to copper

was established, which comprehensively considered both particle impact energy and copper wear mechanism. A series of experiments at various working pressures and impingement angles were conducted for further validation of the proposed wear theory and predictive capability of the wear model. Goodness-of-fit was applied to characterize the matching degree of wear profiles between experimental measurements and numerical simulation. The current research is expected to provide elucidation and reference to actual FJP process optimization of copper by prediction of material removal.

2 Experimental

2.1 FJP device composition

The schematic diagram of the self-designed laboratory scale FJP device is illustrated in Fig. 1(a), which mainly consists of polishing pool, tank, pump, and computer controller. In a typical jet impingement process, a premixed slurry containing water and abrasive was first stored in the tank equipped with a stirrer. The stirrer worked continuously to prevent the abrasive aggregation and sedimentation. Then the slurry was transported from a multi-plunger diaphragm pump at controllable pressure and ejected from the round hole nozzle, which caused apparent material removal on the workpiece surface placed on the fixture. The used slurry in the polishing pool was finally recycled in the tank and mixed well again for the whole experiment. Process parameters such as working pressure, standoff distance and impingement angle illustrated in Fig. 1(b) were adjusted by computer controller to meet a variety of processing demands.

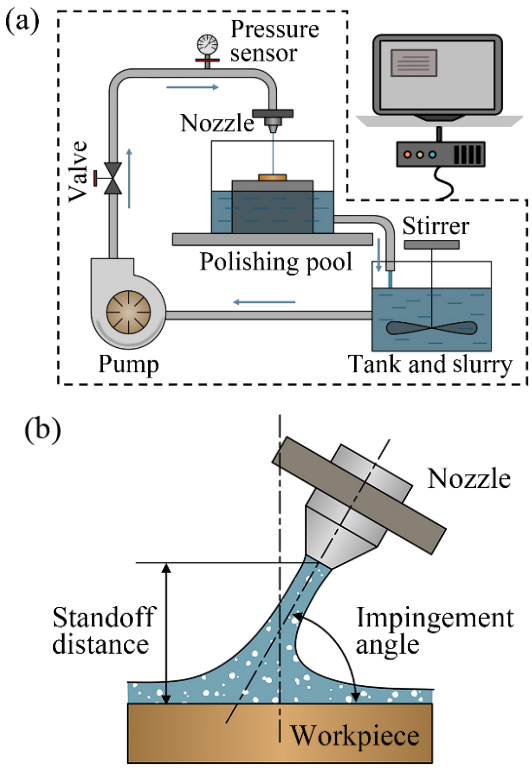

Fig. 1 Schematic diagram of (a) FJP device composition and (b) structural parameters.

2.2 Experimental design

Before FJP experiment, as received oxygen-free flat copper samples (TU1, GB/T 5231-2001, Macklin Ltd., Beijing, China) were chosen as workpieces and were uniformly ground with P600 and P1200 sandpaper sequentially for 30 s under 80 rpm in an automatic polisher (Tegramin-20, Struers, Denmark). A Φ 0.5 mm diameter round hole nozzle in Fig. 2 was utilized for jet generation, which was characterized by optical microscopy (VHX-6000, KEYENCE, Japan). For consistency, the standoff distance was set at 2 mm and the duration of a single impact experiment was 20 min.

For slurry preparation, spherical aluminum oxide particles with the material density of 3,900 kg/m^3 (XWJ Ltd., Hong Kong, China) (Fig. 3(a)) at 5 wt% were dispersed in deionized water with 1 wt% LF900 nonionic surfactant (BASF corp., Germany). As a critical

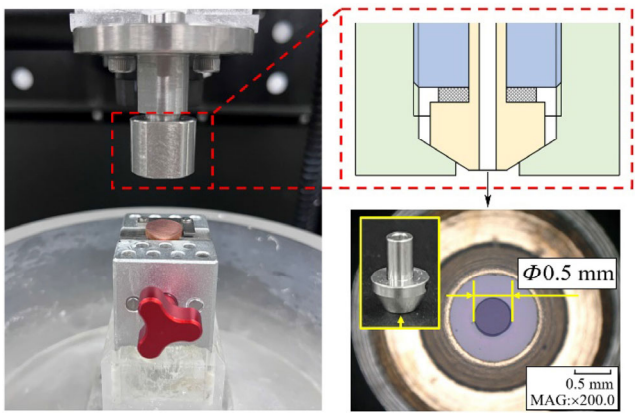

Fig. 2 Experimental nozzle structure and internal diameter measurement.

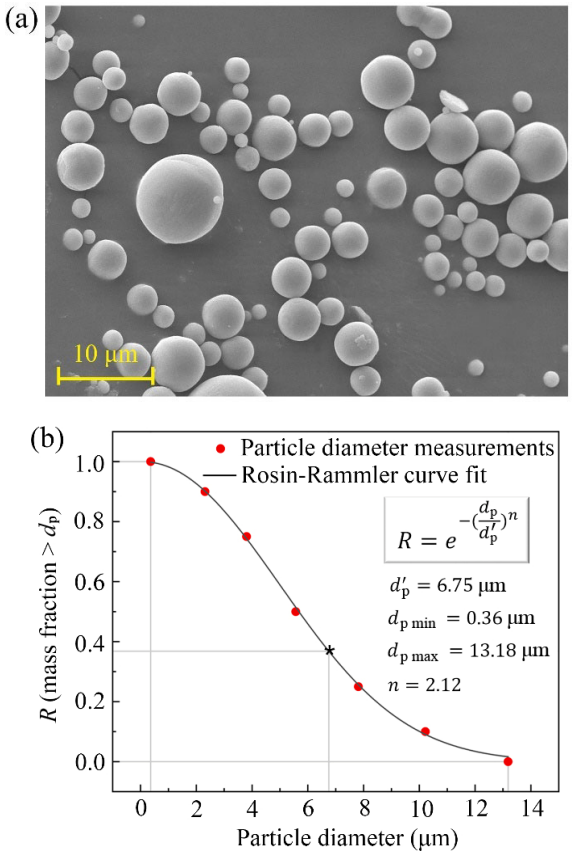

Fig. 3 Particle size distribution of (a) SEM image and (b) Rosin-Rammler curve fit.

consideration in the wear behavior research, the particle size was not uniform according to the scanning electron microscopy (SEM, LYRA 3 FEG-SEM/FIB, TESCAN, Czech) image in Fig. 3(a). The Rosin–Rammler method was adopted to describe the particle size distribution characteristics, which has been demonstrated by various applications for its tremendous adaptability to describe complex particles size distribution states [37–39]. The actual particle size in the experiment measured by laser particle sizer (Hydro2000Mu(A), Malvern, UK) was fitted to the Rosin–Rammler equation in Fig. 3(b) and substituted into the subsequent wear modeling.

A series of jet impingement experiments listed in Table 1 were classified as benchmark and validation respectively for aim of wear modeling and model validation. Benchmark experiment was conducted at 1.2 MPa (jet velocity of 49.0 m/s) with impingement angle of 90°. Validation experiments were designed for three groups. Two of the groups (Validation 1 and Validation 2) altered pressure to 1.0 and 0.8 MPa (jet velocity of 44.7 and 40.0 m/s, respectively), since working pressure directly influenced the impact energy of jet, and leaded to a significant change in material removal rates [40]. The rest one group (Validation 3) was set an impingement angle value of 80° due to a direct effect on the flow field distribution, which caused distinct jet structure [41]. For data reliability, each experiment was repeated three times under the same conditions. The three-dimensional wear morphology and cross-sectional profiles of processed workpiece surfaces were characterized with observation scope of 1× eyepiece and 2.75× objective by white light interference surface topography instrument (ZYGO-NexView, USA).

Table 1 Jet impact experiments conditions.

—	Working pressure (MPa)	Jet velocity (m/s)	Impingement angle (°)
Benchmark	1.2	49.0	90
Validation 1	1.0	44.7	90
Validation 2	0.8	40.0	90
Validation 3	1.2	49.0	80

3 Numerical modeling

3.1 Computational fluid dynamic method

A three-dimensional, incompressible, transient turbulence model was developed to simulate the benchmark impingement experiment by ANSYS Fluent. To consider pulsation effect in the turbulent flow field, time averaging method was applied to achieve reliable calculation results while saving calculation costs [42]. The simulation of gas-liquid-particle flow was conducted by coupling with volume of fluid (VOF) model and discrete phase model (DPM), which were respectively calculated the interfacial variation of gas–liquid and interaction force of liquid-particle. Eulerian–Lagrangian method was performed [21], in which the liquid and air were considered as Eulerian phases, and the Lagrangian particle tracking technique was applied to calculate the forces on individual particle, including drag force, gravitational force, and additional forces (virtual mass force, Saffman's lift force and pressure gradient) [43]:

$$\frac{\mathrm{d}V_\mathrm{p}}{\mathrm{d}t} = F_\mathrm{D}(U - V_\mathrm{p}) + \frac{g(\rho_\mathrm{p} - \rho)}{\rho_\mathrm{p}} + F \tag{1}$$

where V_p and ρ_p are the particle velocity and density; F_D is the drag force per unit particle mass; U is the fluid velocity; ρ is the fluid density and F represents additional forces. $\frac{g(\rho_\mathrm{p} - \rho)}{\rho_\mathrm{p}}$ represents the gravity force. The drag force, F_D is defined as

$$F_\mathrm{D} = \frac{18\mu}{\rho_\mathrm{p} d_\mathrm{p}^2} \frac{C_\mathrm{D}\mathrm{Re}}{24} \tag{2}$$

where μ is the fluid dynamic viscosity; d_p is the particle diameter and Re is the relative Reynolds number, which is defined as

$$\mathrm{Re} = \frac{\rho_\mathrm{p} d_\mathrm{p} (V_\mathrm{p} - U)}{\mu} \tag{3}$$

The drag coefficient C_D defined by Morsi and Alexander [44] was used to calculate the drag force of spherical particles

$$C_\mathrm{D} = \begin{cases} \frac{24}{\mathrm{Re}}(1 + 0.15\mathrm{Re}^{0.687}) & \mathrm{Re} < 1{,}000 \\ 0.44 & \mathrm{Re} < 1{,}000 \end{cases} \tag{4}$$

According to the Lagrangian particle tracking technique, particle-liquid two-way coupling was enabled due to the considered effect of particles on the flow field and DPM sources were updated at each flow iteration. The discrete random walk (DRW) model was activated, which provided a valuable way to account for the particle random motion and the effect of turbulent fluctuations. Convergence analysis of the calculated results of particle impact information was performed by continuously increasing the number of particles incident. Ultimately, 10,000,000 particles were released for tracking until they impacted the target wall and then flowed out of the computational domain to ensure the integrity and stability of the data statistics.

The geometric parameters of the computational domain in Fig. 4 corresponded to the benchmark experiment, which included a nozzle diameter of 0.5 μm and a working distance of 2 mm. The boundary conditions were adopted as velocity-inlet, pressure-outlet, and no-slip wall, respectively. Specifically, the velocity-inlet was set to the same 49 m/s as the benchmark experiment, and the pressure-outlet was set to 0 MPa gauge.

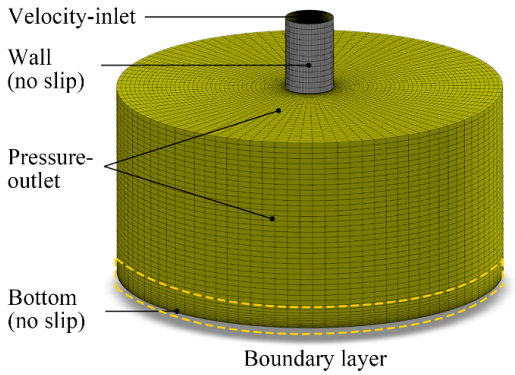

Fig. 4 Geometry model of numerical simulation with boundary conditions.

3.2 Effect of near-wall modeling approach on micron-scale particle motion simulation

Due to the intense turbulent pulsation effect in the jet impact flow field, particle motion is affected by fluid drag force and other additional forces and exhibits irregular trajectories. Unlike particles moving in a straight line in air, particles carried by liquids tend to follow the streamline and separate from it at different locations, which is related to the particle diameter and Stokes number [45]. Among them, small particles are more likely to follow the streamline and be affected by pulsations than large particles as shown in Fig. 5(a).

In the proposed gas-liquid-particle triphasic flow model, the Rosin–Rammler particle size distribution (Fig. 3(b)) was considered. To accurately solve the near-wall region with high velocity and pressure gradients, local refinement of the near-wall mesh is required, mainly by reducing the first cell layer thickness immediately adjacent to the wall (with cell growth rate of 1.2). Therefore, the boundary layer was added to the bottom (Fig. 4), with three kinds of near-wall modeling approaches determined by the bottom $y+$ value illustrated in Table 2. Based on the standard k–ε turbulence model, the first cell layer thickness was determined according to the maximum particle size, the average particle size, and the minimum particle size, which leaded to different near-wall flow

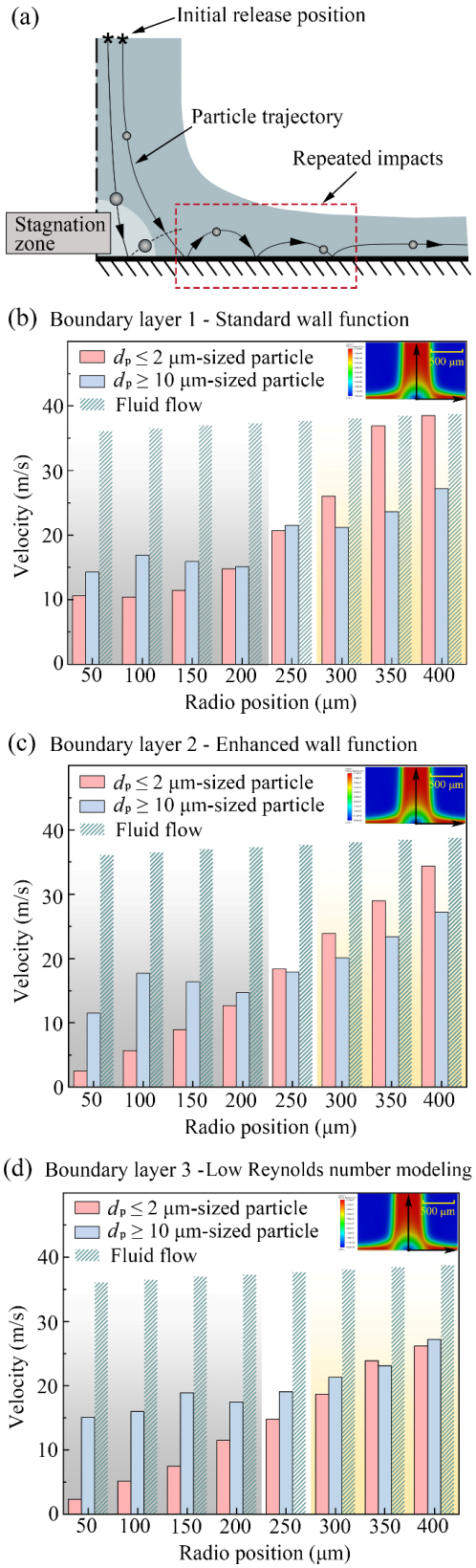

Fig. 5 (a) Schematic diagram of the particle trajectories and particle impact velocity with (b) standard wall function, (c) enhanced wall function, and (d) low Reynolds number modeling.

Table 2 Boundary layer configurations with different near-wall modeling approaches.

Boundary layer configuration	First cell layer thickness (μm)	Maximum $y+$	Near-wall modeling approach
1	13	22	Standard wall function
2	5	11	Enhanced wall function
3	0.5	1	Low Reynolds number modeling

field resolution rates and thus affected the calculation of particle trajectories [46, 47].

The motion information of different-sized particles within 10 μm from the bottom was counted. For obvious comparison, only the impact velocity with particle size less than 2 μm and larger than 10 μm were compared. From Figs. 5(b)–5(d), it can be seen that the large particle velocity was significantly higher than small particle velocity in the radial position < 200 μm range (gray background), which was due to the greater kinetic energy of large particles to penetrate the stagnation zone of the flow field [48]. On the other hand, in the range of radial position > 300 μm (yellow background), the small particles had a higher velocity, which was due to the small particles following the fluid motion.

Apparently, the velocity of small particles was overpredicted in boundary layer configuration 1, especially at radial position = 350–400 μm, which was almost equal to the fluid velocity. This phenomenon was considered as nonphysical impacts of small particle carried by high fluid velocity [46]. In boundary layer configuration 3, the overly fine mesh underestimated the small particle velocity even almost equal to the large particles.

The ideal calculation results were achieved with the boundary layer configuration 2. The small particles lacked sufficient kinetic energy to penetrate the stagnation zone. Along the radial direction, the small particle velocity gradually increased and even exceeded that of the large particles, but is remained lower than fluid velocity. Therefore, the near-wall modeling approach with enhanced wall function was more applicable to the particle motion calculation with the particle size distribution characteristics studied here. All the wear models in this paper would be performed

based on the boundary layer configuration 2, thus obtaining an ideal wall resolution rate to improve the quality of numerical calculation results.

3.3 Wear calculation

In this case, the TIF construction of copper was achieved by substituting the impact information into Oka model for each aluminum oxide particle. Calculation range was started from 'velocity-inlet' and stopped when tracked particles were completely flowed out of the calculation domain. The impact information including particle impact velocity, particle impact angle, and number of repeated impacts were extracted. Oka model can be written as the following equation set [34, 35]

$$E(\alpha) = E_{90} f(\alpha) \tag{5}$$

where $E(\alpha)$ (mm^3/kg) denotes a unit of material volume removed by per mass of particles; E_{90} is the material removal under normal particle impact; $f(\alpha)$ represents the particle impact angle dependence of wear damage.

$$E_{90} = K(Hv)^{k_1}\left(\frac{V_p}{V^*}\right)^{k_2}\left(\frac{d_p}{d^*}\right)^{k_3} \tag{6}$$

$$f(\alpha) = [\sin(\alpha)]^{n_1}\{1 + Hv[1 - \sin(\alpha)]\}^{n_2} \tag{7}$$

$$n_1 = S_1(Hv)^{q_1}, n_2 = S_2(Hv)^{q_2}, k_2 = 2.3(Hv)^{0.038} \tag{8}$$

where K is a constant that regulates the wear depth and needs to be determined experimentally; V_p and V^* are the particle impact velocity and the reference impact velocity; d_p and d^* are the particle diameter and the reference particle diameter, respectively; Hv is the workpiece material Vickers hardness (GPa), its value is 0.9668 for copper measured by Venu's microhardness tester (Qness Q60A+, ShangHai, China).

For initial modeling, a series of default coefficient values were utilized according to literatures, which are shown in Table 3 [34–36]. Significantly, S_1, q_1, S_2, q_2 related to n_1 and n_2 in $f(\alpha)$ needed to be determined by impact conditions such as particle properties, which include particle shape and so on [34]. Whether the coefficients provided in the Oka model (k_2 = 2.30, n_1 = 0.71, n_2 = 2.48) can be used in copper wear calculation was not yet known and would be discussed in subsequent chapters. For comparability of numerical simulation results with experimental data, $E(\alpha)$ can be transformed into a dimensionless quantity by multiplying the material density and employed to represent a new physical quantity. The unit conversion operation was achieved by the definition of K value. To ensure the same wear depth for benchmark experiment and numerical simulation result, the K value of the default Oka model was set to 9,854. In this context, $E(\alpha)$ represented the material removal depth per unit time generated by the slurry containing 5 wt% particles.

Table 3 Coefficient values in the Oka model [34–36].

K	k_1	k_3	S_1	S_2	q_1	q_2	V^* (m/s)	d^* (μm)
Constant	-0.12	0.16	0.71	2.40	0.14	-0.94	104	326

4 Results and discussion

4.1 Comparison of experiment and simulation result

The three-dimensional wear morphology for benchmark experiment shown in Fig. 6(a) presented a ring-shape, which is similar to previous FJP works by glass [48], nickel copper alloy [36], stainless steel [21], and other stiff and brittle material. Such similar phenomena were due to common application of micron-scale particles, which provided insufficient kinetic energy to penetrate the stagnation zone of flow field, resulting in fewer particles impacting the bottom center [40]. The velocity of these particles decayed rapidly, so the wear at bottom center was less severe. Particles outside the stagnation zone repeatedly impacted the target surface with greater kinetic energy, thus forming a ring-shaped wear pattern [48].

Likewise, the ring-shape of wear morphology was simulated by modeling, which is illustrated in Fig. 6(b). However, compared with benchmark experiment result, cross-sectional wear profiles shown in Fig. 7 by Oka model presented apparent incompatibility, which were mainly reflected in three aspects: firstly, the total width of the wear area became broader;

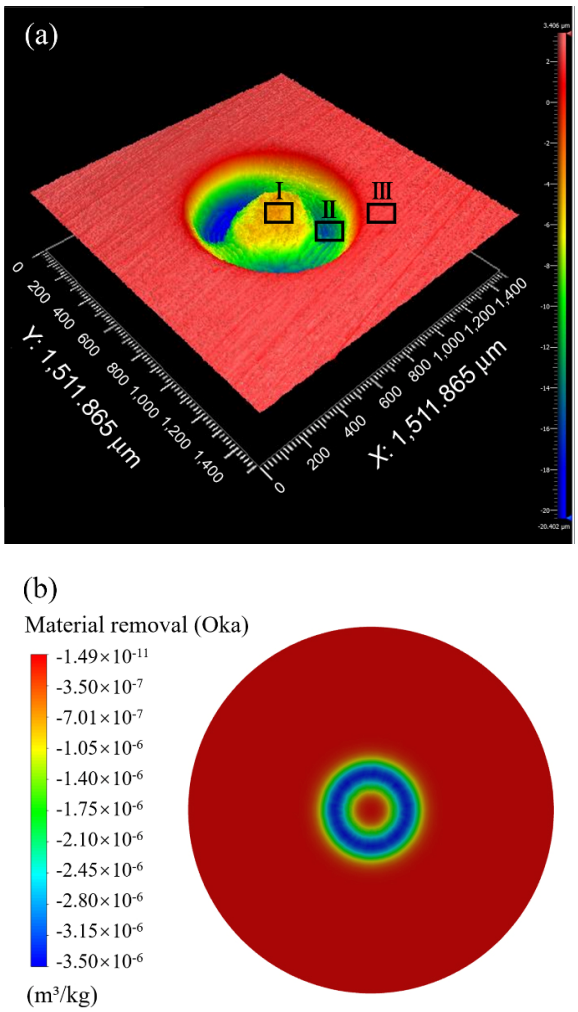

Fig. 6 Surface wear morphology of (a) measured benchmark experiment and (b) numerical simulation.

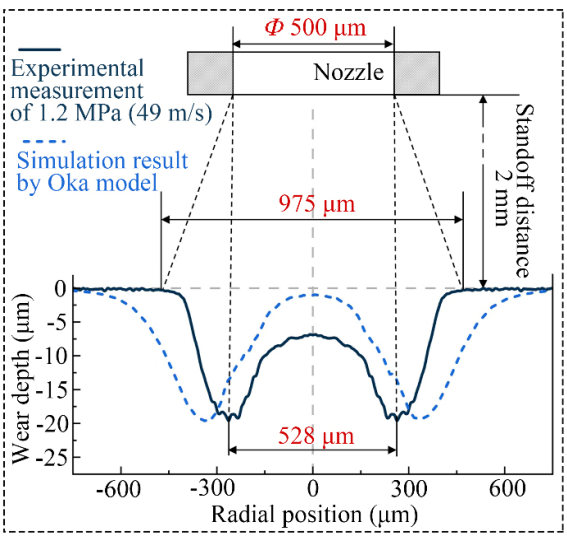

Fig. 7 Cross-sectional wear profiles of experimental measurement and numerical simulation.

secondly, removal peak position (location of the maximum wear occurred) was mismatched to even further away from center; lastly, the central wear rate was almost weakened to disappearance.

More importantly, it can be seen from Fig. 7 that the spacing of the copper removal peaks was approximately equal to the nozzle diameter, and the total width of the wear profile was approximately equal to twice the nozzle diameter. It was not consistent with the literatures on the wear characteristics of stiff and brittle materials, with removal peaks spacing equal to twice nozzle diameter and the total width of the wear profile was equal to four times the nozzle diameter [22, 42]. It reflected that the previous wear model exhibited serious incompatibilities due to the vastly different wear characteristics of copper versus stiff and brittle materials. Hence, the current coefficients of Oka model were no longer applied to copper wear during FJP. The following study would aim at investigation of copper wear mechanism and elimination of incompatibility problem.

4.2 Wear mechanism and wear modeling

The particle velocity can be decomposed into a normal component and a horizontal component. The normal velocity component is responsible for the particle penetration in the workpiece surface (deformation wear) while the horizontal velocity component provides the cutting action as shown in Fig. 8 [22]. Individual

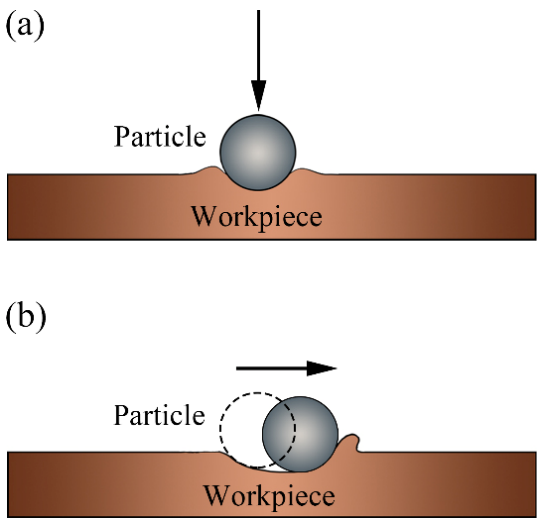

Fig. 8 Schematic diagram of the (a) deformation wear and (b) cutting wear.

particle with high impact angle primarily causes deformation wear since the normal velocity component is larger than the horizontal one. In contrast, individual particle with low impact angle is dominated by cutting wear.

Corresponding to the three regions in Fig. 6(a), respectively, the SEM images of the local wear scars with 20.0k× magnification are shown in Fig. 9. It was noticeable that the wear scar in the central-local area (Region I) and removal peak (Region II) revealed the deformation wear caused by particles at high impact angles. In contrast, for the location near the wear profile edgy (Region III), the wear scars revealed the copper material removal along the fluid flow direction, corresponding to the cutting wear. Apparently, Region III was not the main area of wear occurrence (Fig. 6(a)). From this, it could be inferred that deformation wear at high impact angles caused the major material removal of copper, while cutting wear at low impact angles also occurred but was not the dominant effect.

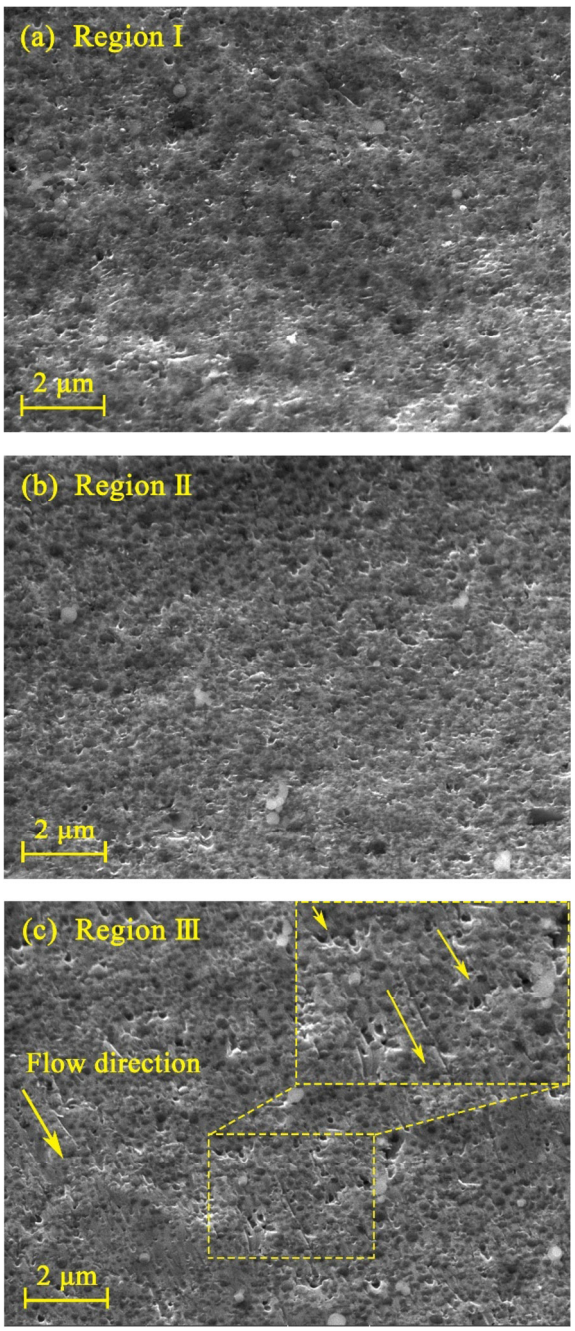

Fig. 9 SEM images of benchmark experiment sample in (a) region I, (b) region II, and (c) region III.

The normal impact energy E_{90} and impact angle dependence $f(\alpha)$ are two significant factors considered in Oka model (Eq. (5)). For normal impact energy, the exponential term $\left(\frac{V_p}{V^*}\right)^{k_2}$ is highly related to impact velocity. In addition, the other two exponential terms $[\sin(\alpha)]^{n_1}$ and $\{1+Hv[1-\sin(\alpha)]\}^{n_2}$, which influenced by particle with different impact angles and workpiece materials, were respectively associated with deformation wear and cutting wear [49]. Oka model suggests that the effects of impact energy and wear mechanisms on material removal are not only related to the hardness of workpiece material, but also to other impact conditions such as particle properties, which is the reason for the incompatibility issue in Fig. 7 [22, 34, 42]. In order to further intensively understand the wear behavior of copper during FJP process, the coefficients k_2, n_1, n_2 were chosen individually for univariate analysis. The values of above coefficients were picked in the range of 0.1–4.0 to cover all of the default values. Normalization of calculated maximum wear was applied to make a more convenient comparison.

With increasing of k_2, the removal peak position tended to moving right to a larger radial position until approached to 400 μm, as shown in Fig. 10(a). This phenomenon was mainly attributed to the increase of power exponent k_2, which would make rapid growing of the term $\left(\frac{V_p}{V^*}\right)^{k_2}$ in mathematical form for both numerical value and slope. Such results would obviously enlarge the influential effect of normal impact energy E_{90} and a more important function

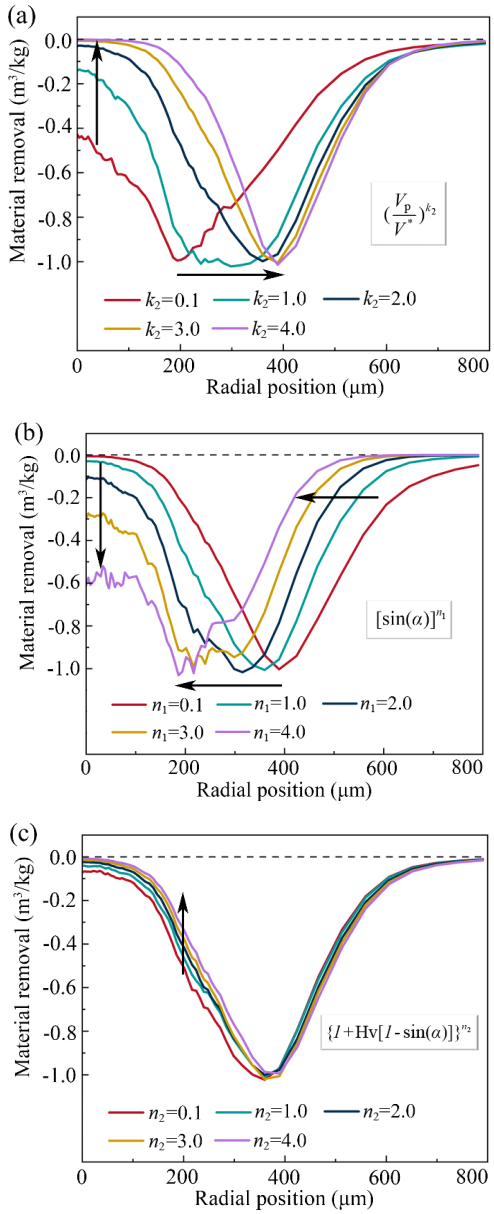

Fig. 10 Effect analysis of coefficients in Oka model on wear numerical simulation.

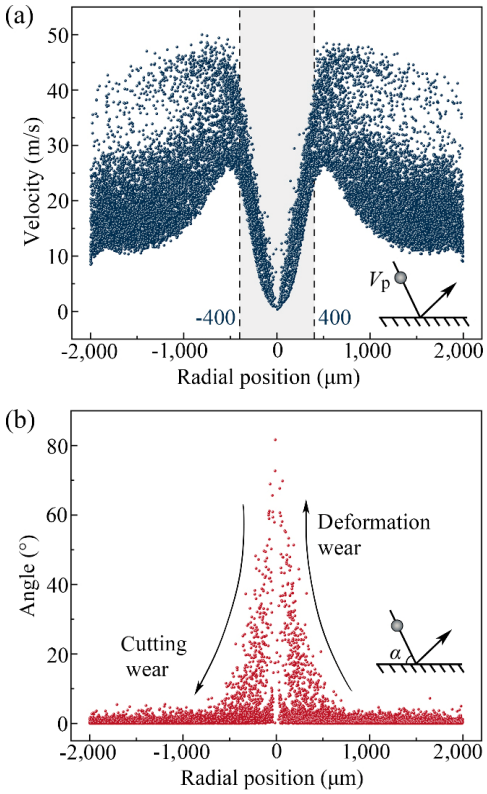

Fig. 11 Micron-scale particles impact velocity and angle distribution at workpiece surface of 1.2 MPa vertical jet impingement.

of impact velocity. On account of the leading role of exponential term $\left(\frac{V_p}{V^*}\right)^{k_2}$, more dependence on the particle impact velocity for material removal rate distribution pattern along the radial was discovered in Fig. 11(a), which forced the removal peak position close to the area where the maximum impact velocity was concentrated. Moreover, the increase of k_2 would cause a sharp drop of central wear rate almost to zero. It was because more contribution of large impact velocity particles (base member V_p in Eq. (6)) with larger k_2 exponential value was stressed to material removal compared with corresponding weaken effect of small impact velocity particles. Therefore, wear was hardly occurred in the area where small impact velocity gathered (grey area in Fig. 11(a)).

Aiming at different wear mechanisms, two exponential terms $[\sin(\alpha)]^{n_1}$ and $\{1+Hv[1-\sin(\alpha)]\}^{n_2}$ are respectively represented deformation wear by high impact angle and cutting wear by low impact angle, as described in previous works [34, 35]. As illustrated in Fig. 10(b), the increase of n_1 gave left shift of radial position, ascending of central removal rate, and shrinking of wear area. The particle impact angle distribution shown in Fig. 11(b) was crucial for explanation of material removal. With increasing of n_1 related to deformation wear, material removal enhancement cause by high impact angle particle was more considered, resulting in the wear occurred in the center area where high impact angle particles concentrated. Meanwhile, central removal rate was enlarged. For cutting wear of low impact angle particle, the calculation was almost neglected due to

corresponding weaken effect of cutting wear, which caused wear area shrinking.

Unlike the variation trend by n_1, the wear rate slight changed with n_2 increasing, as shown in Fig. 10(c). The most possible reason was the area where cutting wear primarily occurred (low particle impact angle concentration in Fig. 11(b)) presented a narrow variation range of impact angle and caused extremely small change of numerical value for $f(\alpha)$. Hence, slight influences on total wear rate $E(\alpha)$ calculation was observed by the change of n_2. Overall, during copper FJP by micron-scale aluminum oxide particle, deformation wear should be adequately evaluated than cutting wear.

With the analysis of the workpiece surface wear scars and the discussion of the micron-scale particle motion information, the coefficients related to the impact kinetic energy and wear mechanism in the wear model in Table 4 can be determined. The rationale was to increase n_1 to account for more deformation wear and decrease n_2 to weaken the effect of cutting wear, combined with the adjustment of the impact kinetic energy effect to make the simulation results fit the experimental measurements. Since the wear study was conducted only for copper material in this paper, and the Eq. (8) was derived from fitting wear data of various workpiece materials, S_1, q_1, S_2, and q_2 are not discussed temporarily. To match the same wear depth as the benchmark experiment, V^* and d^* were set to 10 m/s and 326 μm, respectively, for converting the calculated portions of impact velocity and particle diameter into dimensionless quantities, which were collectively determined to have a final K value of 51. With the proposed coefficients, the ideal match between the numerical simulation and benchmark experimental measurement is depicted in Fig. 12, which resolved the incompatibility of applying default coefficients to the wear behavior during copper FJP.

4.3 Validation of copper wear model

To validate the generalizability of the copper wear model applied in normal impingement FJP process, validation experiments 1 and 2, with separate working pressure values of 1.0 and 0.8 MPa, were proceeded and the corresponding wear model simulations were compared in Fig. 13. Simulations with default Oka model were also conducted and similar incompatibilities were observed, which verified excessive calculation of undesirable cutting wear. Without exception, the proposed copper wear model results intuitively presented an ideal fit with normal impact validation

Table 4 Coefficient values of copper wear model.

K	k_2	n_1	n_2	V^* (m/s)	d^* (μm)
51	4.00	3.50	0.20	10	326

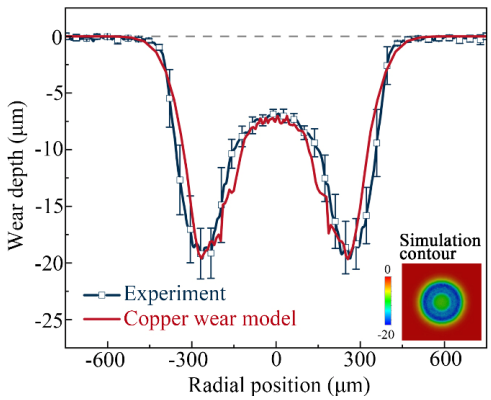

Fig. 12 Cross-sectional wear profiles of benchmark experiment and numerical simulation.

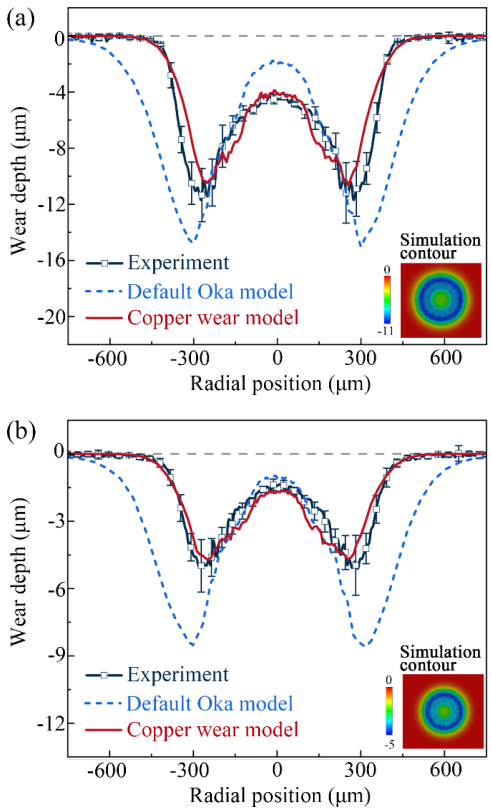

Fig. 13 Validation of the copper wear model reliability at various working pressures.

experiments, including central removal rate, removal peak position, and total width. The goodness-of-fit R^2 was used to describe the fit of numerical simulation results to experimental measurements as shown in Table 5. The value of R^2 ranges from 0 to 1, which a value closer to 1 implied perfect coincidence between the simulated and experimental data [50]. Compared with default Oka model of extremely low R^2 value ranging from 0.15 to 0.53, the modified model showed good R^2 values from 0.92 to 0.97. The goodness-of-fit results manifested favourable quantitative fitness degree of copper wear model and demonstrated predictive capability for copper material removal during normal impingement FJP in 0.8–1.2 MPa.

A further validation experiment 3 for impingement angle of 80° and the corresponding simulation with copper wear model were conducted. Compared with normal impingement experiment with the same maximum depth of two removal peaks, the flow field was unsymmetrical in validation experiment 3, resulting in a deeper removal peak (right-peak, close to nozzle) and another shallower peak (left-peak, away from nozzle), as illustrated in Fig. 14(a). The contour plots of the numerical simulation result by copper wear model in Fig. 14(b) also reflected similar material removal morphology.

The particle impact velocity in Fig. 14(c) and particle impact angle in Fig. 14(d) provided a well explanation for this phenomenon. With the inclination of the nozzle angle, more particles were deposited away from the nozzle side and the particle impact velocity distribution was no longer symmetrical. More importantly, the high particle impact angle occurred only close to the nozzle side. It indicated that the particle impact

Table 5 Goodness-of-fit R^2 of default Oka model and copper wear model.

	Benchmark 1.2 MPa-90°	Validation 1 1.0 MPa-90°	Validation 2 0.8 MPa-90°	Validation 3 1.2 MPa-80°
Default Oka model	0.28	0.53	0.52	0.15
Copper wear model	0.94	0.92	0.93	0.97

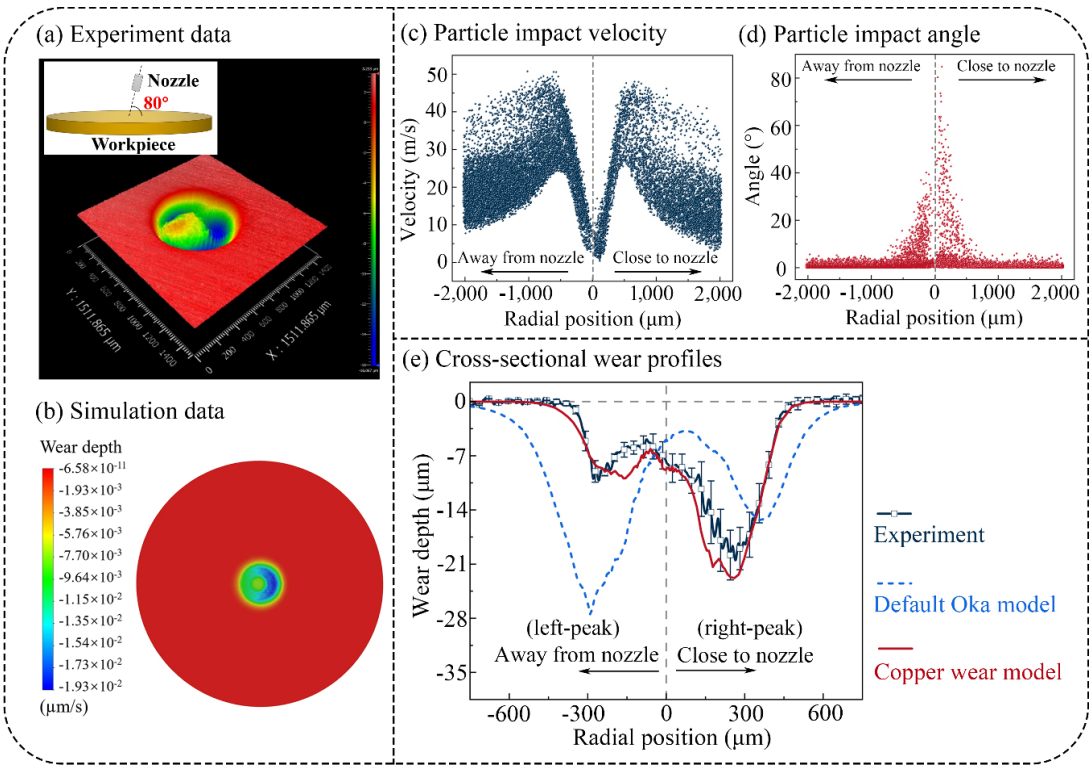

Fig. 14 Validation group 3 with impingement angle of 80°: (a) experiment data of wear, (b) simulation date of wear, (c) particle impact velocity on workpiece surface, (d) particle impact angle on workpiece surface, and (e) cross-sectional wear profiles.

pattern in the benchmark experiment was no longer valid as the jet impingement angle changed. Since the wear model was a statistical and cumulative sum of the material removal caused by each individual particle acting on the workpiece surface, validation group 3 was more convincing to strengthen the reliability judgment of the wear model.

Combined with the wear profile matching in Fig. 14(e) and goodness-of-fit value of 0.97, it was obviously that the proposed wear model is also suitable for copper wear prediction during FJP with tilting nozzle. It is interesting to note that the Oka model caused the exact opposite calculation, which was due to the impact angles at left-peak position were generally lower than right-peak position, resulting in the excessive cutting wear calculation at left-peak. Thus, a comparative study of experiment and simulation at an impingement angle of 80° further demonstrated that deformation wear was more effective for material removal of copper than cutting wear, leading to matching errors of the previous wear model and the ideal matching of the newly proposed copper wear model. More systematic studies with impingement angle alteration will be designed and operated in the future work.

5 Conclusions

A wide difference in the material removal characteristics by copper with stiff and brittle material in fluid jet polishing (FJP) was discovered, mainly in the relative scale relationship between the wear profile and the nozzle diameter. To summarize, the copper wear profile became narrower, in which material removal occurred mainly at the center of the fluid jet with higher particle impact angles. Characterization of the microscopic localized wear scars revealed that deformation wear was the primary mechanism of copper material removal, while cutting wear was also occurring but not causing major material removal.

The matching error existed in previous wear model during FJP calculation was mainly attributed to insufficient consideration of deformation wear. According to evaluation of impact energy and wear mechanism, the parameters of the previous wear model were reassigned to achieve the ideal prediction of the wear profiles for various working conditions. The newly proposed copper wear model fit the experimental measurements with goodness-of-fit up to 0.92–0.97 and filled the gap of copper FJP wear model. This work had been confirmed the feasibility and effectiveness of material removal predicting in copper FJP applications, further refinement and validation should be supplementarily carried out with incorporating other influence factors, including different abrasive and workpiece types, to provide theoretical guidance of wear research during FJP for more material systems in practical applications.

Acknowledgements

This work was supported by the National Natural Science Foundation of China (Grant No. 52175175) and Shenzhen Science and Technology Program (No. JCYJ20220818102809020).

Declaration of competing interest

The authors have no competing interests to declare that are relevant to the content of this article.

References

[1] Wang C J, Zhang Z L, Cheung C F, Luo W, Loh Y M, Lu Y J, Kong L B, Wang S X. Maskless fluid jet polishing of optical structured surfaces. *Precis Eng* **73**:270–283 (2022)

[2] Liu X C, Liang Z W, Wen G L, Yuan X F. Waterjet machining and research developments: a review. *J Adv Manuf Technol* **102**: 1257–1335 (2019)
[3] Zhao X C, Ma L R, Xu X F. Mode transition from adsorption removal to bombardment removal induced by nanoparticle-surface collisions in fluid jet polishing. *Friction* **9**(5): 1127–1137 (2021)
[4] Fähnle O W, Van Brug H, Frankena H J. Fluid jet polishing of optical surfaces. *Appl Opt* **37**(28): 6771–6773 (1998)
[5] Fähnle O W, Van Brug H. Fluid jet polishing: removal process analysis. *Adv Opt Mater* **3739**: 68–77 (1999)
[6] Beaucamp A, Namba Y, Freeman R. Dynamic multiphase modeling and optimization of fluid jet polishing process. *CIRP Annals* **61**(1): 315–318 (2012)
[7] Qiao S, Shi F, Tian Y, Jiao Z Y, Yang P, Zhang W L. Numerical and experimental investigations on NANO-SIO2 jet polishing efficiency by different nozzle structures. *Ceram Int* **48**(11): 15603–15612 (2022)
[8] Zhang H, Zhang X D, Li Z X, Wang P, Guo Z P. Removing single-point diamond turning marks using form-preserving active fluid jet polishing. *Precis Eng* **76**: 237–254 (2022)
[9] Wang C J, Cheung C F, Ho L T, Loh Y M. An investigation of effect of stand-off distance on the material removal characteristics and surface generation in fluid jet polishing. *Nanomanuf Metrol* **3**: 112–122 (2020)
[10] Zhang Z Y, Cui J F, Zhang J B, Liu D D, Yu Z J, Guo D M. Environment friendly chemical mechanical polishing of copper. *Appl Surf Sci* **467**: 5–11 (2019)
[11] Fang F Z, Zhang N, Guo D M, Ehmann K, Cheung B, Liu K, Yamamura K. Towards atomic and close-to-atomic scale manufacturing. *Int J Extreme Manuf* **1**(1): 33 (2019)
[12] Zhu A B, He D Y, He S L, Luo W C. Material removal mechanism of copper chemical mechanical polishing with different particle sizes based on quasi-continuum method. *Friction* **5**(1): 99–107 (2017)
[13] Wang L L, Deng Y, Zou Z X, Xiao Y J, Su G K, Guo Z N. The forming of microgroove in copper foil on multiple laser-induced cavitation impacts. *J Manuf Process* **78**: 82–91 (2022)
[14] Chen H, Guo D, Xie G X, Pan G S. Mechanical model of nanoparticles for material removal in chemical mechanical polishing process. *Friction* **4**(2):153–164 (2016)
[15] Cao Z C, Cheung C F, Ren M J. Modelling and characterization of surface generation in Fluid Jet Polishing. *Precis Eng* **43**: 406–417 (2016)
[16] Schinhaerl M, Rascher R, Stamp R, Smith G, Smith L, Pitschke E, Sperber P. Filter algorithm for influence functions in the computer controlled polishing of high-quality optical lenses. *Int J Mach Tools Manuf* **47**(1): 107–111 (2007)
[17] Chen F J, Wang H, Tang Y, Yin S H, Huang S, Zhang G H. Novel cavitation fluid jet polishing process based on negative pressure effects. *Ultrason Sonochem* **42**: 339–346 (2018)
[18] Zhao J, Huang J F, Wang R, Peng H R, Hang W, Ji S M. Investigation of the optimal parameters for the surface finish of K9 optical glass using a soft abrasive rotary flow polishing process. *J Manuf Process* **49**: 26–34 (2020)
[19] Jafari A, Hattani R A. Investigation of parameters influencing erosive wear using DEM. *Friction* **8**(1): 136–150 (2019)
[20] Cheung C F, Wang C J, Cao Z C, Ho L T, Liu M Y. Development of a multi-jet polishing process for inner surface finishing. *Precis Eng* **52**: 112–121 (2018)
[21] Karimi S, Shirazi S A, McLaury B S. Predicting fine particle erosion utilizing computational fluid dynamics. *Wear* **376**: 1130–1137 (2017)
[22] Cao Z C, Cheung C F. Theoretical modelling and analysis of the material removal characteristics in fluid jet polishing. *Int J Mech Sci* **89**: 158–166 (2014)
[23] Zhang Z L, Cheung C F, Wang C J, Guo J. Modelling of surface morphology and roughness in fluid jet polishing. *Int J Mech Sci* **242**: 107976 (2023)
[24] Farokhipour A, Mansoori Z, Rasteh A, Rasoulian M A, Saffar-Avval M, Ahmadi G. Study of erosion prediction of turbulent gas-solid flow in plugged tees via CFD-DEM. *Powder Technol* **352**: 136–150 (2019)
[25] Buss L, Qi Y L, Heidhoff J, Riemer O, Fritsching U. Towards an understanding of multiphase fluid dynamics of a microfluid jet polishing process: A numerical analysis. *Fluids* **7**(3): 119 (2022)
[26] Finnie I. Erosion of surfaces by solid particles. *Wear* **3**(2): 87–103 (1960)
[27] Bitter J G A. A study of erosion phenomena part I. *Wear* **6**(1): 5–21 (1963)
[28] Bull S J. Using work of indentation to predict erosion behavior in bulk materials and coatings. *J Phys D Appl Phys* **39**(8): 1626–1634 (2006)
[29] Huang C K, Chiovelli S, Minev P, Luo J L, Nandakumar K. A comprehensive phenomenological model for erosion of materials in jet flow. *Powder Technol* **187**(3): 273–279 (2008)
[30] Neilson J H, Gilchrist A. Erosion by a stream of solid particles. *Wear* **11**(2): 111–122 (1968)
[31] Hutchings I M, Macmillan N H, Rickerby D G. Further studies of the oblique impact of a hard sphere against a ductile solid. *Int J Mech Sci* **23**(11): 639–646 (1981)
[32] McLaury B S, Shirazi S A, Shadley J R, Rybicki E F. *Modeling Erosion in Chokes*. New York (USA): American Society of Mechanical Engineers, Fluids Engineering Division (Publication), 1996: 773–782
[33] Meng H C, Ludema K C. Wear models and predictive equations: their form and content. *Wear* **181**:443–457 (1995)

[34] Oka Y I, Okamura K, Yoshida T. Practical estimation of erosion damage caused by solid particle impact: Part 1: Effects of impact parameters on a predictive equation. *Wear* **259**(1–6): 95–101 (2005)
[35] Oka Y I, Yoshida T. Practical estimation of erosion damage caused by solid particle impact: Part 2: Mechanical properties of materials directly associated with erosion damage. *Wear* **259**(1–6): 102–109 (2005)
[36] Wang C J, Cheung C F, Liu M Y. Numerical modeling and experimentation of three dimensional material removal characteristics in fluid jet polishing. *Int J Mech Sci* **133**: 568–577 (2017)
[37] Jia D Z, Li C H, Liu J H, Zhang Y B, Yang M, Gao T, Said Z, Sharma S. Prediction model of volume average diameter and analysis of atomization characteristics in electrostatic atomization minimum quantity lubrication. *Friction* **11**(11): 2107–2131 (2023)
[38] Kumar R, Gopireddy S R, Jana A K, Patel C M. Study of the discharge behavior of Rosin-Rammler particle-size distributions from hopper by discrete element method: A systematic analysis of mass flow rate, segregation and velocity profiles. *Powder Technol* **360**: 818–834 (2020)
[39] Rosin P, Rammler E. Die kornzusammensetzung des mahlgutes im lichte der wahrscheinlichkeitslehre. *Colloid Polym Sci* **67**(1): 16–26 (1934)
[40] Cao Z C, Cheung B C F, Kong L B. Computational fluid dynamics–based analysis of material removal characteristics in fluid jet polishing. *Proc Inst Mech Eng B J Eng Manuf* **230**(6): 1035–1048 (2015)
[41] Anbarasu K G, Vijayaraghavan L, Arunachalam N. Experimental study on surface generation in optical glass with fluid jet polishing process. *Int J Abras Technol* **8**(3): 245–260 (2018)
[42] Mansouri A, Arabnejad H, Shirazi S A, McLaury B S. A combined CFD/experimental methodology for erosion prediction. *Wear* **332**: 1090–1097 (2015)
[43] Information on https://ansyshelp.ansys.com/, 2020.
[44] Morsi S A J, Alexander A J. An investigation of particle trajectories in two-phase flow systems. *J Fluid Mech* **55**(2): 193–208 (1972)
[45] Gnanavelu A, Kapur N, Neville A, Flores J F. An integrated methodology for predicting material wear rates due to erosion. *Wear* **267**(11): 1935–1944 (2009)
[46] Zhang J, McLaury B S, Shirazi S A. Application and experimental validation of a CFD based erosion prediction procedure for jet impingement geometry. *Wear* **394**: 11–19 (2018)
[47] Zhang J, McLaury B S, Shirazi S A. Effect of near wall modeling approaches on solid particle erosion prediction. In: Proceedings of the American Society of Mechanical Engineers, Fluids Engineering Division Summer Meeting, Waikoloa, HI, USA, 2017.
[48] Cao Z C, Wang M, Yan S Q, Zhao C Y, Liu H T. Surface integrity and material removal mechanism in fluid jet polishing of optical glass. *J Mater Process Technol* **311**: 117798 (2023)
[49] Oka Y I, Ohnogi H, Hosokawa T, Matsumura M. The impact angle dependence of erosion damage caused by solid particle impact. *Wear* **203**: 573–579 (1997)
[50] Asadzadeh M Z, Eiböck A, Gänser H P, Klünsner T, Mücke M, Hanna L, Teppernegg T, Treichler M, Peissl P, Czettl C. Tool damage state condition monitoring in milling processes based on the mechanistic model goodness-of-fit metrics. *J Manuf Process* **80**: 612–623 (2022)

Wenjing ZHANG. She received bachelor degree in mechanical engineering in 2020 from Beijing University of Chemical Technology, Beijing, China. Then, she is a postgraduate student in the State Key Laboratory of Tribology in Advanced Equipment at Tsinghua University. Her current research interests include material removal mechanism of fluid jet polishing and wear modeling based on computational fluid dynamics.

Xin ZHANG. She received her Ph.D. degree in chemical engineering & technology in 2019 from Beijing University of Chemical Technology, Beijing, China. She joined the State Key Laboratory of Tribology in Advanced Equipment at Tsinghua University, Beijing, China, from 2020. Her current position is a postdoc of the laboratory. Her research areas cover the ultrafine polishing technology of functional slurry and lignocellulosic functional micro/nano friction materials.

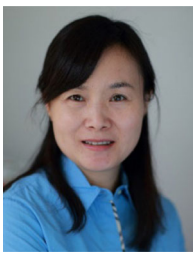

Dan GUO. She received her M.S. degree in engineering mechanics in 1995 from Xi'an Jiaotong University, Xi'an, China, and her Ph.D. degree in engineering mechanics in 1999 from Tsinghua University, Beijing, China. She joined the State Key Laboratory of Tribology in Advanced Equipment at Tsinghua University, Beijing, China, from 1999. Her current position is a professor and the deputy director of the laboratory. Her research areas cover the properties of friction at the micro/nanoscale, mechanism of interaction among nanoparticles and surface in ultra-smooth surface planarization, and the formation and failure of lubricant film in harsh conditions.

Guoshun PAN. He received his M.S. degree in solid mechanics in 1992 from Shandong University of Technology, Shandong, China, and his Ph.D. degree in mechanical engineering in 1998 from China University of Mining and Technology, Beijing, China. He joined the State Key Laboratory of Tribology in Advanced Equipment at Tsinghua University, Beijing, China. His current position is associate professor of the laboratory. His research areas cover the properties of ultra-fine surface processing and micro-nano manufacturing.